Applied Surface Science 674 (2024) 160885

Contents lists available at ScienceDirect

Applied Surface Science

journal homepage: www.elsevier.com/locate/apsusc

Full Length Article

Two-dimensional electron gas isolation mechanism in $Al_{0.2}Ga_{0.8}N$/GaN heterostructure by low-energy Ar, C, Fe ion implantation

Antonino Scandurra [a,b,c,*], Paolo Ragonese [a], Cristiano Calabretta [d], Khadisha Zahra [e], Liam Soomary [e], Fabrizio Roccaforte [f], Giuseppe Greco [f], Nicolò Piluso [d], Maria Eloisa Castagna [d], Ferdinando Iucolano [d], Andrea Severino [d], Elena Bruno [a,b], Salvo Mirabella [a,b]

[a] Department of Physics and Astronomy "Ettore Majorana", University of Catania, Via Santa Sofia 64, 95123 Catania, Italy
[b] Institute for Microelectronics and Microsystems of National Research Council of Italy (CNR-IMM, Catania University Unit), Via Santa Sofia 64, 95123 Catania, Italy
[c] Research Unit of the University of Catania, National Interuniversity Consortium of Materials Science and Technology (INSTM-UdR of Catania), Via S. Sofia 64, 95125 Catania, Italy
[d] STMicroelectronics, Stradale Primosole 50, 95121 Catania, Italy
[e] Kratos Analytical Ltd, A Shimadzu Group Company, Wharfside, Trafford Wharf Road, Manchester M17 1GP, UK
[f] Consiglio Nazionale delle Ricerche – Istituto per la Microelettronica e Microsistemi (CNR-IMM), Ottava Strada, 5 (Zona Industriale) - 95121 Catania (CT), Catania, Italy

ARTICLE INFO

Keywords:
Two-dimensional electron gas
HEMT
Ion implantation
Argon
Carbon
Iron

ABSTRACT

We report a comparative study of the isolation mechanisms of two-dimensional electron gas (2-DEG) in $Al_{0.2}Ga_{0.8}N$/GaN heterostructure by room temperature ion implantation with Ar, C or Fe at 15, 20, 18 keV and fluences of 7×10^{13}, 1×10^{14}, 5×10^{13} cm^{-2}, respectively. The samples were annealed up to 900 °C post-implantation and characterized by X-ray Diffraction, X-ray Photoelectron Spectroscopy, Photoluminescence, Rutherford Backscattering Spectrometry in Channeling mode and Capacitance Voltage profiling. The ion implantation produces unrecoverable crystal lattice damage such as point defects and non-radiative carrier traps level into the band gap of GaN. As a consequence, a decrease in the number of occupied states at the upper side of the valence band of GaN was observed. Moreover, defects accumulation at the near-surface region by annealing at 900 °C was observed. Due to the various defects, the concentration of 2-DEG carriers, after ion implantation, for all three ions investigated, is reduced from 10^{19}-10^{20} to less than 10^{13} —10^{14} cm^{-3}. The 2-DEG isolation was stable up to 900 °C for all three ions, while the non-radiative defects and carrier traps produced were slightly more stable in the case of Fe implantation. The reduction of carrier concentration is responsible for the isolation of 2-DEG.

1. Introduction

The ever-increasing demand of power density and working frequency in telecommunication, as well as in power train and green production of energy applications, pushed the silicon-based IGBT and MOSFETs power devices to their physical limit [1]. Gallium nitride (GaN), among the several wide band gap semiconductors, represents one of the most promising material for the next generation of power electronic devices [2].

The advantages of GaN are related to its superior band-gap, critical electric field for breakdown, high carrier concentration, high electron mobility, and high saturation velocity [3–8].

When a fraction of Ga atoms is replaced in the crystal structure by Al atoms, the growth of AlGaN/GaN heterojunctions is allowed, resulting in a very high sheet carrier density named two-dimensional electron gas (2-DEG). In the presence of the 2-DEG of AlGaN/GaN heterojunctions, High Electron Mobility Transistors (HEMT) can be fabricated. The mechanisms producing the carrier density at 2 DEG are represented by the piezoelectric polarization at the AlGaN/GaN interface due to the mismatch of the crystal lattice parameters, as well as to the different electronegativity of Al, Ga and N [9,10].

The formation of crystal defects in AlGaN/GaN by ion implantation,

* Corresponding author at: Department of Physics and Astronomy "Ettore Majorana", University of Catania, via Santa Sofia 64, 95123 Catania, Italy.
E-mail address: antonino.scandurra@dfa.unict.it (A. Scandurra).

https://doi.org/10.1016/j.apsusc.2024.160885
Received 3 May 2024; Received in revised form 24 July 2024; Accepted 31 July 2024
Available online 7 August 2024

which can be exploited for the electrical isolation of 2-DEG, where required, has been widely reported by several authors [11–18]. Isolation by ion implantation is a planar process, has several advantages compared to the mesa process, such as higher breakdown voltage for the same gate-to-drain distance and the reduction of gate leakage current [19]. Several types of ions implantation have been reported for the isolation of the 2-DEG such as Xe^+, Kr^+, Ar^+, C^+, Al^+, N^+, O^+, Fe^+, F^+, B^+ and other [11–18]. The defect creation and evolution in GaN is a complex process, still not fully understood.

Several authors have reported that the stability of 2-DEG isolation is guaranteed over a wide temperature range, generally between 400 and 1200 °C [11–18]. Some data, especially regarding the temperature at which the isolation remains stable, in the order of 10^{11} Ω/□, seem to disagree with each to other. In addition, the ion energy used in the implantation is often high, in the order of hundreds of keV, and the fluences up to 10^{17} cm^{-2}. Moreover, multiple implants are proposed to cover large thickness of the semiconductor and to obtain uniform damage profiles [13,16].

2-DEG isolation mechanism for most implanted ions, in particular inert noble gas ions, is attributed to the formation of crystal damage [12]. The ions of noble gases essentially act with a ballistic mechanism. Due to the damage created by heavy ions such as $^{84}Kr^+$ in AlGaN/GaN lattice, the 2-DEG isolated by ion implantation showed better thermal stability than implant isolation by e.g., $^{40}Ar^+$. It has been reported that heavy ion implantation of inert gas ($^{84}Kr^+$) is a viable solution for the fabrication of thermally stable planar AlGaN/GaN HEMTs even up to 800 °C under long-term isochronous annealing [12].

Taube and co-workers reported that double ion implantation with C produce 2-DEG isolation characterized by a thermal stability up to 600 °C [13]. Carbon is a deep acceptor in GaN. The authors in the work maintained the vacancy concentration, no less than 10^{20} cm^{-3}.

Pągowska and co-workers reported that Fe ion implantation produces an isolation of the 2-DEG stable up to 1100 °C. The formation of high resistance and thermally stable isolating regions in GaN needs the Fe concentration to be at least around 1×10^{19} cm^{-3} [16].

Theoretical study by Umeda and co-workers reported that Fe implanted atoms in Ga sites of GaN form deep levels. Accordingly, the resistivity of the Fe ion-implanted regions was found over 10^{10} Ω/□ even after the annealing at 1200 °C [17].

In our previous paper, we described the effects on the 2-DEG isolation by Ar ion implantation at relatively low energies of 15, 22, 5 and 60 keV and fluence of 7×10^{13} [20]. We used an experimental procedure based on wafer level characterization of the defects by photoluminescence (PL) and the isolation measurement by capacitance–voltage profiling. We found that the electrical isolation was stable up to 900 °C.

This work provides a contribution to understanding the mechanisms of defect formation and isolation of 2-DEG by implantation of Ar, C or Fe ions. According to the literature, we chose C and Fe, and compared the results with those obtained for Ar, since these three species are expected to produce 2-DEG isolation by different mechanisms. The mechanisms were studied in detail using X-ray diffraction (XRD), photoluminescence (PL), X-ray photoelectron spectroscopy (XPS), channeling mode Rutherford backscattering spectrometry (RBS/C) and capacitance–voltage profiles (CV).

Ar, C or Fe, were implanted into 18 nm $Al_{0.2}Ga_{0.8}N$/GaN heterostructures at different ion energies and doses. We still used a simplified procedure based on wafer level defect characterization and measurements of the electrical isolation by mercury probe. This approach does not require the fabrication of test patterns which need thermal annealed metal contacts. Thus, we avoid or, at least, minimized the effects at the semiconductor–metal pad interfaces in the electrical characterization of the 2-DEG. The implanted samples were annealed at 600, 750 and 900 °C, to characterize the defect evolution and the thermal stability of the isolation. The temperature range was chosen to cover conditions encountered in most processes involved in the manufacturing of a HEMT device, i.e., the temperatures typical for the formation of ohmic contacts to the AlGaN/GaN heterostructure.

2. Experimental

The investigated samples consist of $Al_{0.2}Ga_{0.8}N$ 18 nm thin layer, with a GaN capping layer 1 nm thin, deposited onto intentionally carbon doped n-type GaN, by metal–organic chemical vapor deposition (MOCVD). Six-inches Si semiconductor wafers (111) were used as substrates for the growth of the $Al_{0.2}Ga_{0.8}N$/GaN heterostructure (Fig. 1a). The wafers were grinded to a thickness of 400 μm and then sawed into 20 mm × 20 mm dice. The ion implantation process was simulated by SRIM software [21]. The ion energies were chosen in order to have peak concentration of the vacancy defects located at a depth close to the $Al_{0.2}Ga_{0.8}N$/GaN interface, i.e., 19 nm. The cross section (not to scale) of the heterostructure is schematized in Fig. 1. Fig. 1b highlights the region affected by the ion implantation. The ion implantations were done at room temperature. Ar was implanted at 15, 22.5 and 60 keV and 7×10^{13} cm^{-2} of fluence; C at 20 keV and 1×10^{14} of fluence; Fe at 18 keV and 5×10^{13} cm^{-2} of fluence, respectively. The implantations were done by an ion implanter equipped with Cockroft-Walton linear accelerator, operating in the voltage range between 10 and 400 kV, (High Voltage Engineering Europe BV). Typical current of the ion implantations of Ar, C and Fe was ~ 70nA.

After ion implantation the samples were annealed at 600, 750, 900 °C, respectively, under N_2 flux at ambient pressure, for 15 min in a Carbolite Gero tubular oven. Then, the samples were cooled down to room temperature under N_2 flux and removed from the oven.

XRD analyses were done by a Smartlab Rigaku diffractometer, employing the Cu Kα X-ray source with a rotating anode operated at 45 kV and 200 mA.

XPS analyses were done by the Kratos AXIS Supra Instrument, equipped with monochromatic Al Kα (1486.6 eV) and Ag Lα (2984.3 eV) X-ray sources. XPS high resolution spectra were acquired over an area of 700 μm × 300 μm employing the Al Kα X-ray source at a power of 450 W and an emission current of 30 mA. XPS depth profiling were obtained by sputtering the sample with a 10 keV Ar^+_{1000} cluster ions and acquiring the Al 2p, Ga 2p, O 1 s, C 1 s and Ga LMM signals at the various etching steps. The etching crater was 2 mm × 2 mm and the analyzed area 110 μm of diameter. The binding energy scale was corrected for the charging up effects, fixing the C 1 s adventitious component at 285 eV.

PL characterization was done at room temperature by Nanometrics RPM 2000 Photoluminescence Mapper. The PL spectra were excited by Nd-YAG laser source operating at a wavelength of 266 nm.

RBS characterization was done by the 3.5 MV HVEE ((High Voltage Engineering Europe, Netherlands) Singletron Accelerator System. The experimental setup of the RBS/C analyses was optimized to have the maximum sensitivity towards crystallographic damage in the first 20 nm of the samples. The primary He^+ ion beam, at a current of 150nA, was accelerated at 1 MeV of energy, and 40 μC of total charge was used. The Si detector was placed at a backscattering angle of 165°, with a 1 mm slit in front of it by reaching a solid angle of 1 mstr. The system energy resolution (detector, beam energy, electronic chain) and dead time were checked during each measurement with a dedicated voltage pulser, showing that the energy resolution was 16 keV and dead time below 1 %.

3. Results

Fig. 2 shows the simulations of total vacancy concentration distributions obtained by each ion implantation process by Ar, C, Fe, at energies of 15, 20, 18 keV, and fluences of 7×10^{13}, 1×10^{14}, 5×10^{14} cm^{-2}, respectively. The ion energies were selected to have the peak of defect concentration close to the 2-DEG. Furthermore, the ion fluences were selected to obtain defect concentrations above 10^{21} cm^{-3} over a thickness of approximately 40 nm for Ar and Fe and 85 nm for C.

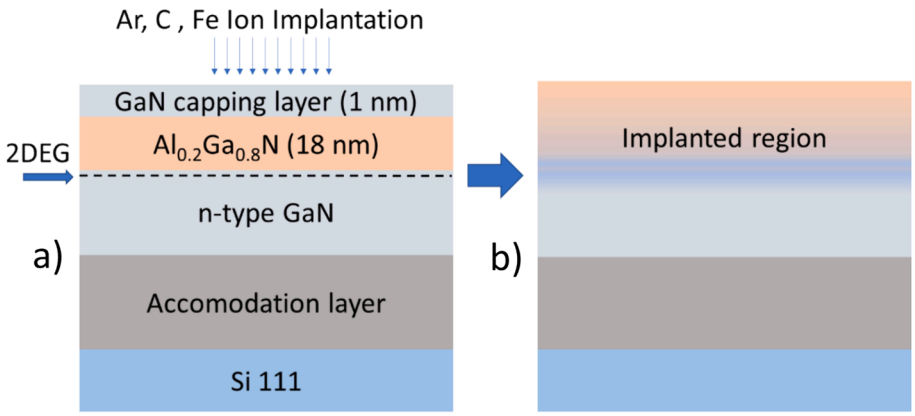

Fig. 1. (a) Cross section of the $Al_{0.2}Ga_{0.8}N$/GaN heterostructure; (b) representation of the region involved by the ion implantation. Note that the thicknesses of the various layers are not to scale.

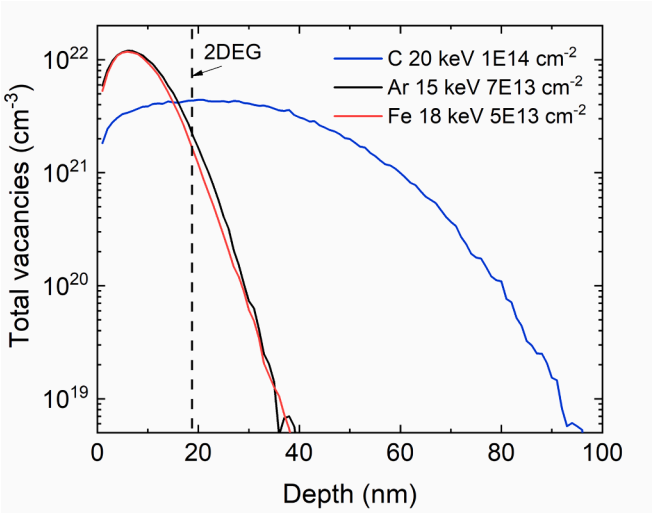

Fig.2. Simulation by SRIM software of the total vacancy depth distributions induced in $Al_{0.2}Ga_{0.8}N$/GaN heterostructure by implantation with: Ar at 15 keV, 7×10^{13} cm^{-2} of fluence; C at 20 keV, 1×10^{14} cm^{-2} of fluence; Fe 18 keV, 5×10^{13} cm^{-2} of fluence, respectively.

Fig. 3a-c shows the XRD diffractograms in the 2θ range of 71-75°, of the $Al_{0.2}Ga_{0.8}N$/GaN virgin (green line), implanted with Ar, C, Fe, (black, blue and red solid lines) and post-implant annealed at 900 °C (black, blue and red dashed lines). The reported range comprises the reflections peaks assigned to GaN 0004 and $Al_{0.2}Ga_{0.8}N$ 0004, respectively [13]. The 0004 peaks give a better balance between intensity and peak separation than 0002 peaks [22]. In the virgin sample, the GaN 0004 peak is centered at 73.10°, while the peak of $Al_{0.2}Ga_{0.8}N$ 0004 is centered at 73.70°. In the diffractograms of the Ar and C implanted samples, the peaks are centered at 73.00° and 73.60°, respectively. In carbon post-implant annealed sample, the peak positions remain at 73.00 and 73.60°. Conversely, in the diffractogram of the Ar post-implant annealed sample the peaks positions were found once again at 73.10° and 73.60°. In the diffractogram of the Fe implanted sample the peak positions are not affected by implantation, neither by post-implant annealing. Taube and coworkers observed a new damage peak GaN 0004, located at about 72.60°, in addition to the undamaged peak located at 72.80°, appearing in $Al_{0.16}Ga_{0.84}N$/GaN after ion implantation with carbon at 250 keV 4×10^{13} and 520 keV, 5×10^{13} cm^{-2}, or with aluminum at 300 keV, 1.4×10^{13} cm^{-2} and 800 keV, 10^{13} cm^{-2}, respectively [13]. Turos observed damage peaks after ion implantation of GaN with Ar ion at 320 keV. The peak (GaN 0002) is located at 2θ 0.1° lower diffraction angles from the undamaged substrate peak. The shift is a measure of the lattice parameter variation and, thus, the residual stress in the bombarded region of the crystal [23,24]. Fig. S1 of Supplementary Information shows the simulation obtained by VESTA software [25] of the 0004 reflection of unstrained GaN. The structure parameters of GaN wurtzite reported by Xu and co-worker have been used [26,27]. The peak is centered at 2θ of 72.85°. Thus, the experimental value of 0004 reflection position of virgin sample we found is attributable to a compressed layer of GaN. The shift we observed in the GaN 0004 after ion implantation may be interpreted as the results of an unresolved convolution of the peak assigned to undamaged crystal with that of the damaged GaN. The damage peak indicates the existence of a defects-rich layer with larger lattice parameter than that of virgin material.

Fig. 4 shows the Ga 2p and Al 2p core level spectra of virgin and Ar, C, Fe post-implant annealed samples at 900 °C. The spectra were acquired from the unetched surfaces, before the ion-etching by $Ar\,1000^{+}$ at 10 keV, employed for the depth profiling. The Ga $2p_{3/2}$ and Ga $2p_{1/2}$ spin–orbit doublets of virgin, Ar and C post-implant annealed samples are centered at 1117.8 eV and 1144.8 eV of binding energy, respectively. The values of binding energy are assigned to Ga atoms bonded to N atoms in the GaN compound and are in good agreement with those found by Qin and co-workers [28]. In the Fe post-implant annealed sample, the Ga $2p_{3/2}$ and Ga $2p_{1/2}$ peaks were found at 1118.3 eV and 1145.5 eV, respectively, that can be attributable to a Ga-O oxidation state [28]. The corresponding Al 2p spectra were fitted by single Gaussian components with FWHM of 1 eV, centered at 73.65, 73.51, 73.63, 73.62 eV, for virgin, Ar, C and Fe post-implant annealed sample, respectively. The spectra of Al 2p can be entirely attributed to Al-N bonds of AlGaN, and are in good agreement with the literature data [28]. Notable, we did not find any component attributable to the bonds of aluminum with oxygen, which excludes oxidation phenomena of the samples that could be expected in annealing at 900 °C, even in presence of oxygen trace. The results confirm the high stability against oxidation of GaN and AlGaN alloys [29].

Fig. 5 shows the normalized Ga $L_2M_{45}M_{45}$ Auger structure of the virgin and post-implant annealed samples, recorded at various depths after Ar^{+}_{1000} sputtering. The Ga $L_2M_{45}M_{45}$ spectrum excited by Al Kα is close to the N 1 s core level component. At the depths of 0.45, 9 and 13.6 nm the Auger spectra of the post-implant annealed samples, deviate from the spectrum of the virgin sample. At the depths 9 and 13.6 nm, according to Fig. 2, the highest concentration of defects produced by ion implantation are present. At the depth 0.45 nm we expect a high concentration of defects corresponding to that of the sub-surface. In particular, a reduction of the intensity of the Auger signal at the high side of the kinetic energy may be observed. Therefore, the analysis of the $L_2M_{45}M_{45}$ Auger spectra gives information on the crystal damage. At depths corresponding to the peak concentration of defects, the Auger

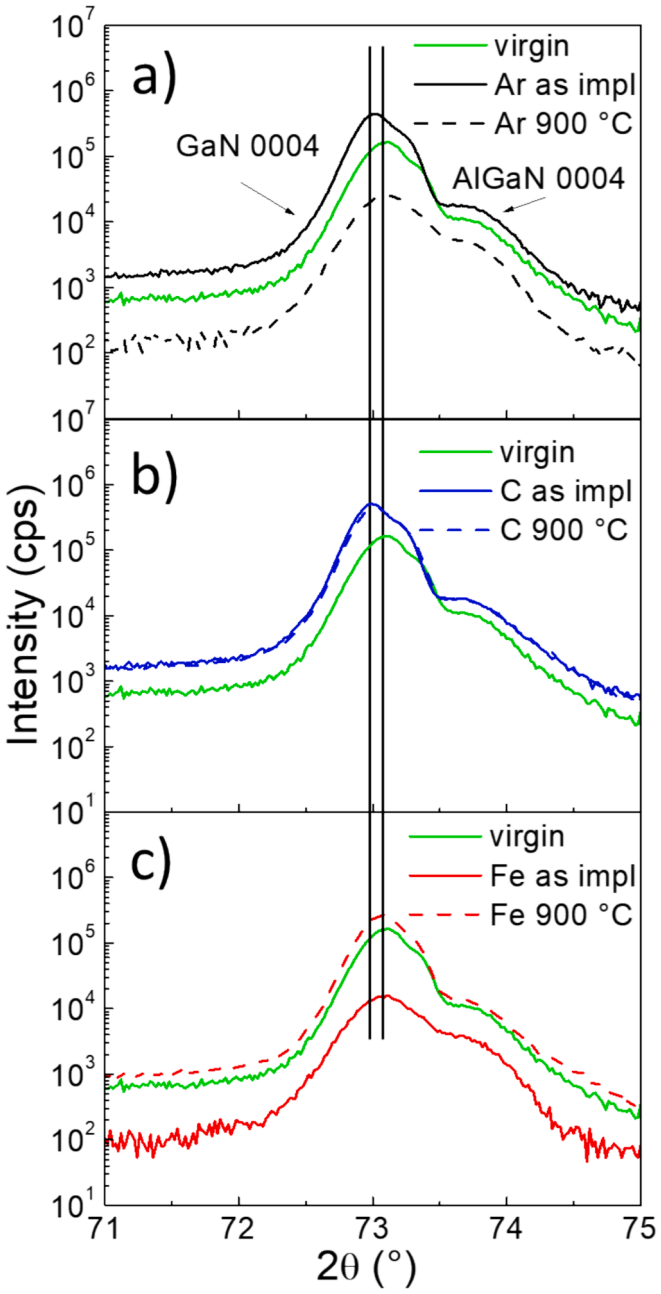

Fig. 3. Diffractograms of $Al_{0.2}Ga_{0.8}N$/GaN virgin, as implanted and post-implant annealed at 900 °C: (a) Ar at 15 keV, 7×10^{13} cm^{-2} of fluence; (b) C at 20 keV, 1×10^{14} cm^{-2} of fluence; (c) Fe 18 keV, 5×10^{13} cm^{-2} of fluence. The vertical lines were added to help the eye to visualize the centroid of the GaN 0004 peaks.

spectrum is deviated less in the sample implanted with C, compared to the samples implanted with Ar or Fe, due to the lower concentration of defects, according to its smaller fluence and its lower atomic mass.

Fig. 6 shows the PL spectra in the range of 300–650 nm of wavelength of virgin, Ar, C and Fe, as implanted and post-implant annealed $Al_{0.2}Ga_{0.8}N$/GaN samples at 600, 750 and 900 °C. The spectrum of the virgin sample shows an intense and narrow peak centered at about 363.3–363.8 nm, which is assigned to radiative recombination at band edge (BE) of GaN, and a less intense peak centered at about 335 nm, assigned to radiative recombination at BE of $Al_{0.2}Ga_{0.8}N$. Moreover, a broad band which extends between 500 and 650 nm is assigned to the yellow band (YB) [30]. The YB is attributed to donor to acceptor radiative recombination process at the defects consisting of carbon impurities in the nitrogen substitution position (C_N) [31], as well as to substitution oxygen (O_N) and gallium vacancy (V_{Ga}) recombination [32,33].

The photoluminescence peak assigned to BE of GaN, in the samples implanted with C or Fe, undergoes the greatest reduction in intensity with respect to the virgin sample, compared to the sample implanted with Ar. In the samples annealed at 900 °C, a slight increase in the intensity of the BE peak in the order C > Ar > Fe is noted, showing a greater stability of the non-radiative defects produced by the Fe implantation compared to that of C or Ar. In all the spectra of the implanted samples, the intensities of the peaks assigned to BE of GaN and $Al_{0.2}Ga_{0.8}N$ are reduced by approximately two orders of magnitude. The significant reduction of BE peaks is attributed to the defects produced by the ion implantation, that consist of non-radiative centers [9]. The intensities of the BE peaks assigned to GaN and $Al_{0.2}Ga_{0.8}N$ are no longer restored to the that of virgin sample, even at 900 °C, demonstrating that defects produced near the BE, assigned to non-radiative centers, are stable up to this temperature.

Carrier concentration of virgin, annealed, implanted and post-implant annealed samples were obtained by Mott-Schottky elaboration of the capacitance–voltage profiles [20]. Table 1 shows the carrier concentrations, Nmax, at the 2-DEG of virgin and as function of the ion energy, fluence and the post-annealing temperature. For comparison, we reported the carrier concentrations found in the samples that only underwent thermal annealing. The carrier concentration has been obtained by elaboration of the CV profiles by the Mott-Schottky Equation (1):

$$N_{CV} = \frac{C^3}{e\varepsilon_0\varepsilon}\frac{dV}{dC} \quad (1)$$

where N_{CV} is the carrier concentration, C is the capacitance, V the voltage, e the elemental charge, ε_0 the dielectric constant of vacuum and ε the relative dielectric constant.

Annealing at 600 °C induces an improvement in the crystal quality due to the reduction of the concentration of point defects and dislocations, allowing the detection of a greater carrier concentration of 2-DEG with respect to the reference sample. Further increase in the annealing temperature up to 900 °C has the opposite effect by inducing the partial modification of the AlGaN layer. Conversely, the ion implantation produces a significant stable reduction of the carrier concentration of about six to seven orders of magnitude and the corresponding isolation up to 900 °C, with respect to the virgin sample.

Fig. 7 shows the RBS/C spectra of the virgin (scattered data in Fig. 7a), Fe implanted at 18 keV, 5×10^{13} cm^{-2} of fluence (scattered data in Fig. 7b), and Fe 18 keV, 5×10^{13} cm^{-2} of fluence post-implant annealed at 900 °C (scattered data in Fig. 7c) samples. The intense peaks located at about 810 keV are attributed to the backscattering induced by the surface defects. The RBS spectra were simulated by McChasy code [34], trying several point defect concentrations profiles. The best simulation of the spectrum of the implanted sample was obtained considering a point defect concentration profile of 7 % at. in the first 10 nm and 1 % at. up to 20 nm deep (inset in Fig. 7b). Fig. 7c shows the simulation of post-implant annealed sample, where we hypothesized the accumulation of point defects towards the surface as consequence of the post-implant annealing. In this case the best simulation was obtained assuming a defect concentration profile of 25 % at. in 5 nm and 2 % at. up to 20 nm deep (inset in Fig. 7c). Interesting, the surface peak increases with respect to the situation of Fig. 7a and 7b. The defects cause an increasing of the surface peak in the RBS/C spectra as well as the appearing of a backscattering peak at energies just below the surface peak. The main difference in the RBS/C spectra is highlighted in the comparison (Fig. 7d) and concerns the surface peak intensity, that is greater in the spectrum of post-implant annealed sample (cyan) with respect to both virgin (magenta) and implanted sample (dark yellow). This result is assigned to the formation of surface damage. Notably, the backscattered He^+ ions are due to the scattering by Ga atoms. Indeed,

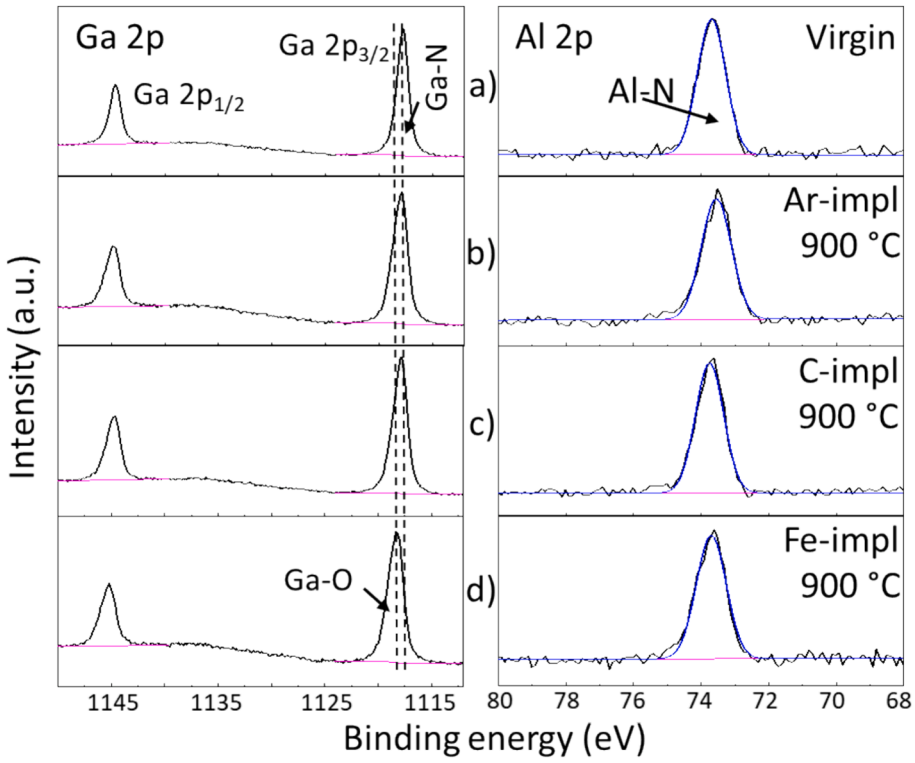

Fig. 4. X-ray photoelectron spectra of Ga 2p and Al 2p core level regions of the unetched surfaces of (a) $Al_{0.2}Ga_{0.8}N$/GaN virgin; (b) Ar-implanted at 15 keV, 7×10^{13} cm^{-2} of fluence and post-implant annealed at 900 °C; (c) C-implanted at 20 keV, 1×10^{14} cm^{-2} of fluence and post-implant annealed at 900 °C; (d) Fe-implanted at 18 keV, 5×10^{13} cm^{-2} of fluence and post-implant annealed at 900 °C. The dashed vertical lines identify the positions relative to the binding energies of $Ga2p_{3/2}$ assigned to Ga-N and Ga-O.

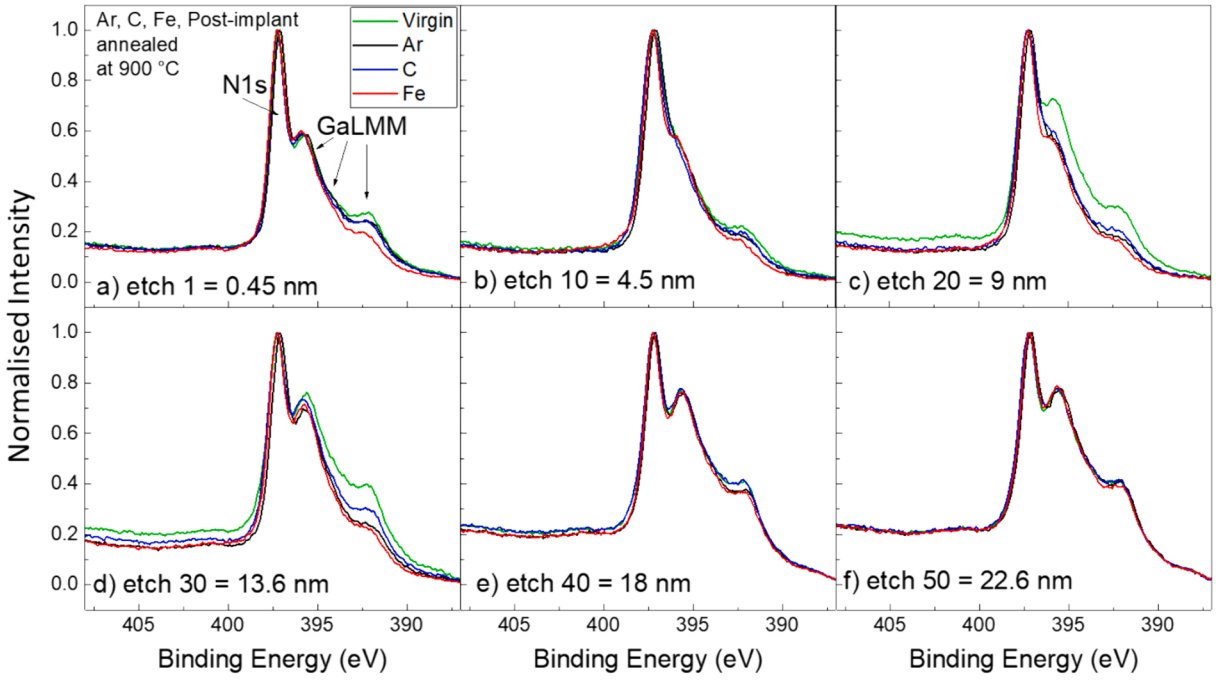

Fig. 5. Normalized $GaL_2M_{45}M_{45}$ Auger spectra, recorded at various depths, of $Al_{0.2}Ga_{0.8}N$/GaN virgin and Ar-implanted at 15 keV, 7×10^{13} cm^{-2} of fluence, C-implanted at 20 keV, 1×10^{14} cm^{-2} of fluence and Fe-implanted at 18 keV, 5×10^{13} cm^{-2} of fluence and post-implant annealed at 900 °C. At depths of 9 and 13.6 nm the Auger spectra of post-implant annealed samples are significantly lower than of virgin.

the Rutherford scattering cross section depends on the atom mass and the Ga atoms represent the principal scattering center. The absence or very low de-channeling, which is produced primarily by dislocation defects, is evidenced in the comparison of the spectra. This is an indication that the damage produced in our samples, in the portion of thickness sampled by RBS technique, are mainly point defects [35].

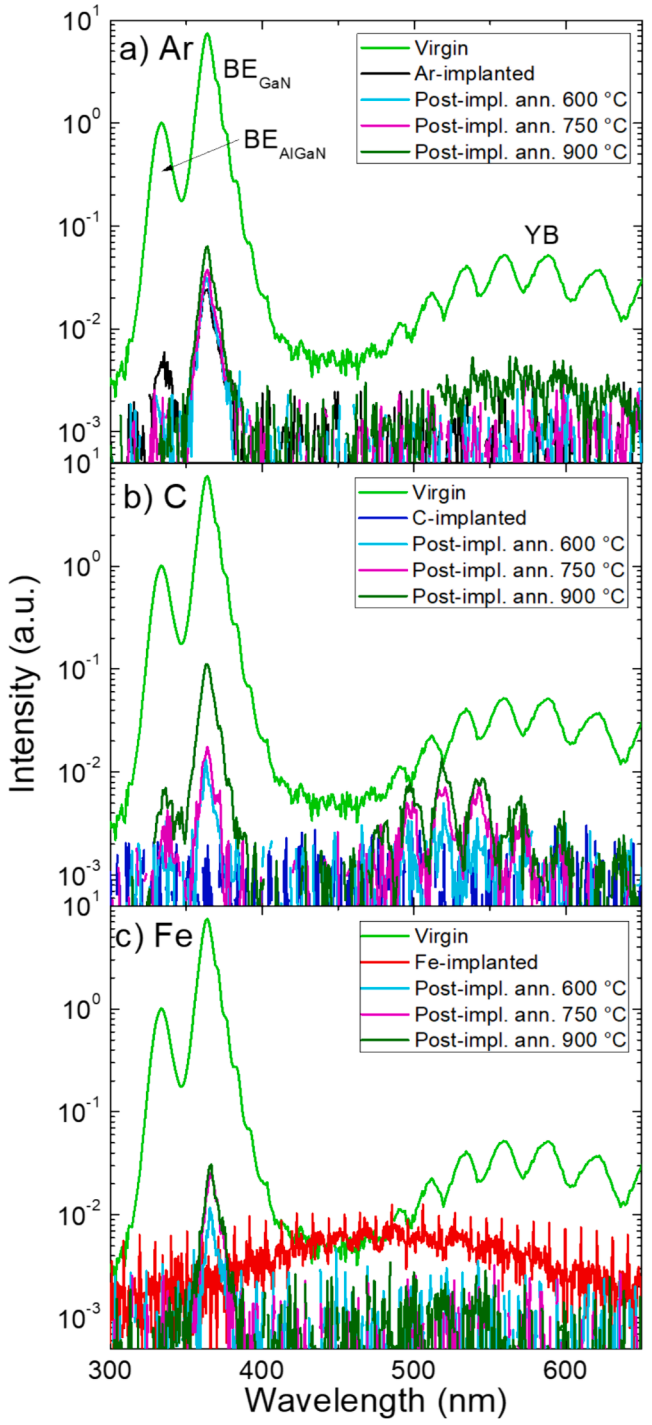

Fig. 6. Photoluminescence spectra of $Al_{0.2}Ga_{0.8}N$ /GaN virgin and (a) Ar-implanted at 15 keV, 7 × 10^{13} cm^{-2} of fluence; (b) C-implanted at 20 keV, 1 × 10^{14} cm^{-2} of fluence; (d) Fe-implanted at 18 keV, 5 × 10^{13} cm^{-2} of fluence, post-implant annealed at 600, 750 and 900 °C.

Fig. 8a compares the RBS/C spectra of the $Al_{0.2}Ga_{0.8}N$/GaN virgin, Ar, C, Fe post-implant annealed at 900 °C. Interesting, an increase in surface peak intensity is observed in all spectra, with that relating to Fe slightly more intense. Fig. 8b shows the area of the surface damage peak as a function of ion and annealing temperature. This peak increases with the annealing temperature, which can be explained by the damage diffusion to the surface. We propose the following hypothesis, that the annealing causes the accumulation of the defect to the surface. This is further verified by the increasing surface peak and that at 900 °C, the lattice is not entirely restored.

Table 1
Carrier concentration of the 2-DEG in the investigated samples, obtained by Mott-Schottky elaboration of the CV profiles.

Sample ID	Ion	Energy (keV)	Fluence	Annealing temperature (°C)	Nmax (cm^{-3})
Virgin	–	–	–	–	(4.0 ± 0.2) × 10^{19}
Annealed only	–	–	–	600	(6.7 ± 0.3) × 10^{20}
Annealed only	–	–	–	750	(3.7 ± 0.2) × 10^{19}
Annealed only	–	–	–	900	(3.9 ± 0.2) × 10^{19}
Ar 15 keV	Ar	15	7·10^{13}	As implanted	<10^{13}
Ar 15 keV	Ar	15	7·10^{13}	600	~10^{14}
Ar 15 keV	Ar	15	7·10^{13}	750	~10^{14}
Ar 15 keV	Ar	15	7·10^{13}	900	~10^{14}
Ar 22.5 keV	Ar	22.5	7·10^{13}	600	<10^{14}
Ar 60 keV	Ar	60	7·10^{13}	600	<10^{14}
C 20 keV	C	20	10^{14}	As implanted	<10^{14}
C 20 keV	C	20	10^{14}	600	<10^{14}
C 20 keV	C	20	10^{14}	750	<10^{14}
C 20 keV	C	20	10^{14}	900	<10^{14}
Fe 18 keV	Fe	18	5·10^{13}	As implanted	<10^{14}
Fe 18 keV	Fe	18	5·10^{13}	600	<10^{14}
Fe 18 keV	Fe	18	5·10^{13}	750	<10^{14}
Fe 18 keV	Fe	18	5·10^{13}	900	<10^{14}
Fe 30 keV	Fe	30	5·10^{13}	600	<10^{14}
Fe 80 keV	Fe	80	5·10^{13}	600	<10^{14}

4. Discussion

The results of the characterizations obtained by the several techniques suggest different mechanisms, induced by the implantation of Ar, C, Fe ions, which lead to the formation of defects in the $Al_{0.2}Ga_{0.8}$/GaN heterostructure and, therefore, the 2-DEG isolation. One mechanism responsible of the 2-DEG isolation is represented by an increase in the lattice parameters of GaN compared to the virgin sample [23]. The simulations show that the GaN layer in the virgin heterostructure is compressed, according to the literature [24]. Implantation with Ar and C produces a clearly visible effect in the increasing of the crystal lattice parameters. This increase can be explained through a reduction in the mechanical compressive stress, exerted on the GaN, by the $Al_{0.2}Ga_{0.8}N$ layer which, in turn, partially relaxes its original tensile stress after ion implantation [24]. The partial relaxation of the initial stresses of both $Al_{0.2}Ga_{0.8}N$ and GaN reduces the piezoelectric polarization that contributes to the formation of the 2-DEG carrier concentration. In the post-implant annealed samples, in the case of argon, the conditions of virgin sample are restored, while in the case of C the effect remains. In the samples implanted with Fe, no significant variations were observed in the XRD pattern. We do not have a simple explanation of this finding, but it can be hypothesized that argon can be released as gas in the post-implant annealed sample while carbon cannot. Fe, owing to its high atomic mass, has a projected range closest to the interface with the $Al_{0.2}Ga_{0.8}N$ layer, thus the damaged layer is shallower than in other cases. Furthermore, Fe atoms can replace Ga atoms at substitutional sites [17]. According to Usman and co-workers, in particular for Ar and Fe ions, ion implantations of GaN is expected to induce the formation of a significantly higher concentration of nitrogen defects than gallium defects, due to the smaller displacement energy of N compared to Ga [36].

The analysis of the Ga $2p_{1/2}$-Ga $2p_{3/2}$ and Al 2p XPS core levels did not show significant oxidation of the surface. The Fe post-implant annealed sample shows the presence of a more pronounced defect-rich, partially oxidized shallow layer. The $L_2M_{45}M_{45}$ Auger process involves the levels $3p_{1/2}$ (L_2) and 3d ($M_{45}M_{45}$). In GaN compound we can assume an interaction of the hybridized 3d and 4p orbitals of gallium with 2 s and 2p of nitrogen in the valence band [28]. Therefore, the

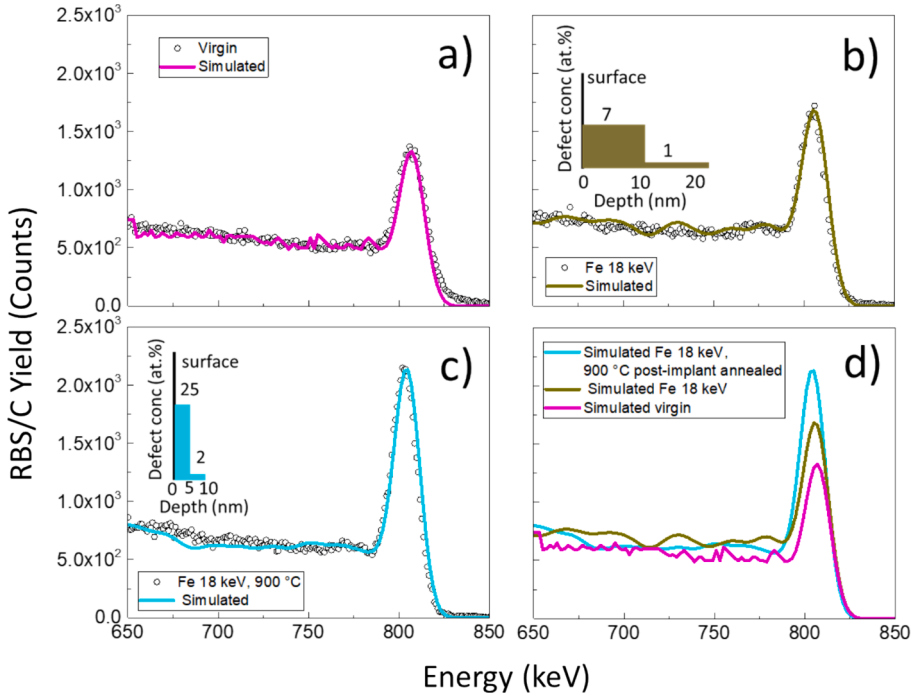

Fig. 7. RBS/C spectra of $Al_{0.2}Ga_{0.8}N$/GaN: (a) virgin; (b) Fe implanted at 18 keV, 5×10^{13} cm^{-2} of fluence; c) Fe 18 keV, 5×10^{13} cm^{-2} post-implant annealed at 900 °C. The scattered data (empty circles) refer to the experimental spectra; colored lines refer to the simulated spectra by McChasy code. The inset in b and c represent the point defect concentration profiles used in the simulation; (d) comparison of the simulated spectra of Fig. 7a-c. Conditions: energy of He^+ beam: 1 MeV; $\phi = 15°$.

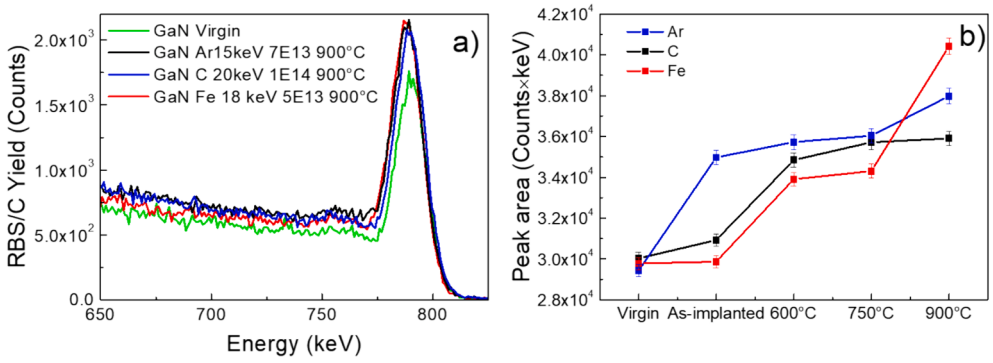

Fig. 8. RBS/C of $Al_{0.2}Ga_{0.8}N$/GaN: a) comparison of the spectra virgin and Ar-implanted at 15 keV, 7×10^{13} cm^{-2} of fluence, C-implanted at 20 keV, 1×10^{14} cm^{-2} of fluence and Fe-implanted at 18 keV, 5×10^{13} cm^{-2} of fluence and post-implant annealed at 900 °C; b) surface damage peak area of $Al_{0.2}Ga_{0.8}N$/GaN virgin and Ar-implanted at 15 keV, 7×10^{13} cm^{-2} of fluence, C-implanted at 20 keV, 1×10^{14} cm^{-2} of fluence and Fe-implanted at 18 keV, 5×10^{13} cm^{-2} of fluence, post-implant annealed at 600, 750 and 900 °C.

$L_2M_{45}M_{45}$ Auger process involves electrons present in the valence band. The modification of the Ga $L_2M_{45}M_{45}$ Auger spectra, shows that ion implantation produces the reduction in the density of occupied states in the upper side of the valence band. This means that the disorder induced by the ion implantation reduces the number of occupied states in the high energy region of the valence band [37]. According to this interpretation, we can observe that the reduction of the number of occupied states in the valence band is maximum for Fe in a region close to the surface, while it is comparable for C and Ar. This experimental result is in good agreement with that obtained theoretically by Umeda and co-workers [17]. At the depths corresponding to the highest defects concentrations, i.e. between 9 and 13 nm, the reduction in the density of occupied states is slightly less for C than for Ar or Fe, in agreement with the lower fluence and its lower atomic mass.

The reduction in the density of occupied states at the valence band may be associated with the formation of defect centers and carrier traps characterized by non-radiative recombination of pairs. This is indicated by the strong reduction of the PL peaks assigned to the BE of GaN and $Al_{0.2}Ga_{0.8}N$, respectively.

The RBS/C analyses showed low de-channeling as expected due to the low fluence implantation. Furthermore, from the rise of the surface peak intensity after post-implant annealing, we can hypothesize the accumulation of point defects in a region closest to the surface. The simulations by McChasy code are in agreement with the hypothesis that point defect concentration increases in the 5 nm below the surface upon post-implant annealing. This result is in agreement with Turos et al., showing an accumulation of nitrogen vacancy in a region close to the surface upon ion bombardment with Ar at 320 keV of GaN [23]. Moreover, at 900 °C, the lattice and electronic structure of the virgin $Al_{0.2}Ga_{0.8}N$/GaN are not restored. This phenomenon is more pronounced in the Fe post-implant annealed sample, demonstrating that the damage in the first 20 nm of the sample persists and cannot be restored.

The peak areas assigned to the surface defects of the RBS/C spectra of the post-implant Ar, C, Fe samples annealed at 900 °C are higher than that of the virgin sample spectrum. As a consequence of the formation of lattice and electronic structure defects, all the implanted samples show a reduction of 2-DEG carrier concentration by six to seven orders of magnitude. The reduction of the carrier concentration is stable up to 900 °C and is the basis of the isolation of the 2-DEG.

5. Conclusions

In this paper we described the isolation mechanisms of 2-DEG in $Al_{0.2}Ga_{0.8}N$/GaN heterostructure by low energy, low fluence Ar, C or Fe ion implantation. We adopted a time and cost-saving methodology based on wafer level spectroscopic characterization of defects formation and evolution. Moreover, capacitance–voltage profiling was used to characterize the 2-DEG carrier concentration. The techniques we used for the characterization, show that the defects formation by ion implantation at the conditions we used are stable up to 900 °C. This temperature is well beyond that typically required to withstand in device manufacturing processes, such as metal annealing for the formation of gate and source contacts, e.g. 600 °C. In all the implanted and post-implant annealed samples, we observed a reduction of the carrier concentration of six to seven orders of magnitude with respect to the virgin sample. We have demonstrated that low ion energy implantation (few keV) is suitable to achieve high temperature stable 2-DEG isolation. Our study shows that Ar, C, Fe ion implantations are able to produce a stable isolation in the temperature range of 600–900 °C. Moreover, the defects produced by Fe implantation are more stable than the other ions. The choice of the type of ion can be dictated by the conditions of the device manufacturing processes; it increases the design flexibility of the individual process steps in the fabrication of an AlGaN/GaN HEMT. The present study represents an important technological guide, since the implantation conditions and effects produced, necessary for effective and stable electrical isolation of AlGaN/GaN 2-DEG, have been described in detail.

CRediT authorship contribution statement

Antonino Scandurra: Writing – review & editing, Writing – original draft, Investigation, Formal analysis, Data curation, Conceptualization. **Paolo Ragonese:** Investigation, Formal analysis. **Cristiano Calabretta:** Investigation. **Khadisha Zahra:** Investigation. **Liam Soomary:** Investigation. **Fabrizio Roccaforte:** Conceptualization. **Giuseppe Greco:** Conceptualization. **Nicolò Piluso:** Conceptualization. **Maria Eloisa Castagna:** Methodology, Conceptualization. **Ferdinando Iucolano:** Supervision, Methodology, Conceptualization. **Andrea Severino:** Methodology, Conceptualization. **Elena Bruno:** Writing – review & editing, Investigation, Data curation, Conceptualization. **Salvo Mirabella:** Writing – review & editing, Investigation, Funding acquisition, Data curation, Conceptualization.

Declaration of competing interest

The authors declare that they have no known competing financial interests or personal relationships that could have appeared to influence the work reported in this paper.

Data availability

Data will be made available on request.

Acknowledgements

The Project “Sviluppo di semiconduttori ad ampia banda proibita per dispositivi di potenza e telecomunicazione avanzata” CUP: E65F21002570005 – D.M. n. 1062 del 10 agosto 2021 Asse IV, Azione IV.4 “Dottorati e contratti di ricerca su tematiche dell’innovazione” del PON “R&I” 2014-2020 is acknowledged for financial support. The Bionanotech Research and Innovation Tower (BRIT) Laboratory of the University of Catania (Grant no. PONa3_00136 financed by the MIUR) for the Smartlab diffractometer facility.

Appendix A. Supplementary material

Supplementary data to this article can be found online at https://doi.org/10.1016/j.apsusc.2024.160885.

References

[1] F. Roccaforte, P. Fiorenza, G. Greco, R.L. Nigro, F. Giannazzo, F. Iucolano, M.J.M. E. Saggio, Microelectron. Eng. 187 (2018) 66.
[2] J. He, Wei-C. Cheng, Q. Wang, K. Cheng, H. Yu, Y. Chai, Recent Advances in GaN-Based Power HEMT Devices, Adv. Electron. Mater. 7 (2021), 2001045.
[3] F. Ren, S.J. Pearton, Recent advances in wide-bandgap semiconductor biological and gas sensors, Semiconductor Device-Based Sensors for Gas, Chemical, and Bio Applications, CRC Press, Boca Raton London New York, 2011, pp. 43–96.
[4] N. Herbecq, I.R. Jeune, A. Linge, M. Zegaoui, P.O. Jeannin, N. Rouger, F. Medjdoub, Above 2000V breakdown voltage at 600 K GaN-on-silicon high electron mobility transistors, Phys. Status Solidi A 213 (2016), 873–877.
[5] T. Ueda, Y. Uemoto, T. Tanaka, D. Ueda, GaN transistors for power switching and millimeter-wave applications, Int. J. High Speed Electron. Syst. 19 (2009) 145–152.
[6] B. Li, X. Tang, J. Wang, K.J. Chen, Optoelectronic devices on AlGaN/GaN HEMT platform, Phys. Status Solidi A 213 (2016) 1213–1221.
[7] H. Sun, A.R. Alt, S. Tirelli, D. Marti, H. Benedickter, E. Piner, C.R. Bolognesi, Nanometric AlGaN/GaN HEMT performance with implant or mesa isolation, IEEE Electron Device Lett. 32 (2011) 1056–1058.
[8] U.K. Mishra, L. Shen, T.E. Kazior, Y.-F. Wu, GaN-based RF power devices and amplifiers, Proc. IEEE. 96 (2008) 287–305.
[9] A.M. Nahhas, Review of AlGaN/GaN HEMTs Based Devices, American Journal of Nanomaterials 7 (2019) 10–21. https://pubs.sciepub.com/ajn/7/1/2.
[10] F. Zeng, J.X. An, G. Zhou, W. Li, H. Wang, T. Duan, L. Jiang, H. Yu, A Comprehensive Review of Recent Progress on GaN High Electron Mobility Transistors: Devices, Fabrication and Reliability, Electronics 7 (2018) 377, https://doi.org/10.3390/electronics7120377.
[11] H. Sakurai, T. Narita, K. Kataoka, K. Hirukawa, K. Sumida, S. Yamada, K. Sierakowski, M. Horita, N. Ikarashi, M. Bockowski, Effects of the sequential implantation of Mg and N ions into GaN for p-type doping, Appl. Phys. Express 14 (2021) 111001. https://iopscience.iop.org/article/10.35848/1882-0786/ac2ae7.
[12] S. Arulkumaran, K. Ranjan, G.I. Ng, P.P. John Kennedy, T.N. Murmu, S.T. Bhat, Thermally stable device isolation by inert gas heavy ion implantation in AlGaN/GaN HEMTs on Si, J. Vacuum Sci. & Technol. B 34 (2016), 042203 Doi: 10.1116/1.4955152.
[13] A. Taube, E. Kamińska, M. Kozubal, J. Kaczmarski, W. Wojtasiak, J. Jasiński, M. A. Borysiewicz, M. Ekielski, M. Juchniewicz, J. Grochowski, M. Myśliwiec, E. Dynowska, A. Barcz, P. Prystawko, M. Zając, R. Kucharski, A. Piotrowska, Ion implantation for isolation of AlGaN/GaN HEMTs using C or Al, Phys. Status Solidi A 212 (2015) 1162–1169, https://doi.org/10.1002/pssa.201431724.
[14] C.F. Lo, T.S. Kang, L. Liu, C.Y. Chang, S.J. Pearton, I.I. Kravchenko, O. Laboutin, J. W. Johnson, F. Ren, Isolation blocking voltage of nitrogen ion-implanted AlGaN/GaN high electron mobility transistor structure, Appl. Phys. Lett. 97 (2010) 262116.
[15] J.Y. Shiu, J.C. Huang, V. Desmaris, C.T. Chang, C.Y. Lu, K. Kumakura, T. Makimoto, H. Zirath, N. Rorsman, E.Y. Chang, Oxygen ion implantation isolation planar process for AlGaN/GaN HEMTs, IEEE Electron Device Lett. 28 (2007) 476–478, https://doi.org/10.1109/LED.2007.896904.
[16] K. Pągowska, M. Kozubal, A. Taube, R. Kruszka, M. Kaminski, N. Kwietniewski, M. Juchniewicz, A. Szerling, The interplay between damage and chemical induced isolation mechanism in Fe^{+} implanted AlGaN/GaN HEMT structures, Mater Sci Semicond Process 127 (2021) 105694, https://doi.org/10.1016/j.mssp.2021.105694.
[17] H. Umeda, T. Takizawa, Y. Anda, T. Ueda, T. Tanaka, High-Voltage Isolation Technique Using Fe Ion Implantation for Monolithic Integration of AlGaN/GaN Transistors, IEEE Trans. on Electron Devices 60 (2013) 771–775. https://doi.10.1109/TED.2012.2230264.
[18] S. Tan, X. Deng, B. Zhang, J. Zhang, Thermal stability of F ion-implant isolated AlGaN/GaN heterostructures, Sci. China Phys. Mech. Astron. 61 (2018) 127311, https://doi.org/10.1007/s11433-018-9312-7.
[19] M. Sun, H.-S. Lee, B. Lu, D. Piedra, T. Palacios, Comparative breakdown study of mesa and ion-implantation-isolated AlGaN/GaN high-electron-mobility transistors on Si substrate, Appl. Phys. Express 5 (2012) 074202, https://doi.org/10.1143/APEX.5.074202.
[20] A. Scandurra, M. Testa, G. Franzò, G. Greco, F. Roccaforte, M.E. Castagna, C. Calabretta, A. Severino, F. Iucolano, E. Bruno, S. Mirabella, Isolation of bidimensional electron gas in AlGaN/GaN heterojunction using Ar ion implantation, Mater Sci Semicond Process 168 (2023) 107871, https://doi.org/10.1016/j.mssp.2023.107871.

[21] J. Ziegler, The Stopping and Range of Ions in Matter, SRIM-2013.00 software http://www.srim.org.
[22] Zhou Sheng-Qiang1, Wu Ming-Fang1 and Yao Shu-De, A Practical Guide for X-Ray Diffraction Characterization of Ga(Al, In)N Alloys, Chinese Phys. Lett. 22 (2005), 1984 DOI 10.1088/0256-307X/22/8/045.
[23] A. Turos, On the mechanism of damage buildup in gallium nitride, Radiat Eff. Defects Solids 168 (2013) 431–441, https://doi.org/10.1080/10420150.2013.777445.
[24] R.N. Kyutt, M.P. Shcheglov, V.Y. Davydov, A.S. Usikov, Deformation of AlGaN/GaN superlattice layers according to x-ray diffraction data, Phys. Solid State 46 (2004) 364–370, https://doi.org/10.1134/1.1649438.
[25] VESTA software, available online at: https://jp-minerals.org/vesta/en/download.html, accessed on 6 June, 2024.
[26] Y.N. Xu, W.Y. Ching, Electronic, optical, and structural properties of some wurtzite crystals, Phys. Rev. B 48 (1993) 4335–4351.
[27] crystallographic parameters of GaN wurtzite, available online at: https://www.crystallography.net/cod/result.php, accessed on 6 June, 2024.
[28] X. Qin, H. Dong, J. Kim, R.M. Wallace, A crystalline oxide passivation for Al_2O_3/AlGaN/GaN, Appl. Phys. Lett. 6 (2014) 141604, https://doi.org/10.1063/1.4897641.
[29] D.A. Zatsepin, D.W. Boukhvalov, A.F. Zatsepin, Quality assessment of GaN epitaxial films: Acidification scenarios based on XPS-and-DFT combined study, Appl. Surf. Sci. 563 (2021) 150308, https://doi.org/10.1016/j.apsusc.2021.150308.
[30] Y.-N. Zhong, S.-W. Tang, Y.-M. Hsin, Determination of Suitable Indicators of AlGaN/GaN HEMT Wafer Quality Based on Wafer Test and Device Characteristics, Phys. Status Solidi A 215 (2018) 1700628, https://doi.org/10.1002/pssa.201700628.
[31] M. Takahashi, A. Tanaka, Y. Ando, H. Watanabe, M. Deki, M. Kushimoto, S. Nitta, Y. Honda, K. Shima, K. Kojima, S.F. Chichibu, K.J. Chen, H. Amano, Suppression of Green Luminescence of Mg-Ion-Implanted GaN by Subsequent Implantation of Fluorine Ions at High Temperature, Phys. Status Solidi B 257 (2020) 1900554, https://doi.org/10.1002/pssb.201900554.
[32] X. Li, P.W. Bohn, J.J. Coleman, Impurity states are the origin of yellow-band emission in GaN structures produced by epitaxial lateral overgrowth, Appl. Phys. Lett. 27 (1999) 4049–4051, https://doi.org/10.1063/1.125532.
[33] H.Z. Xu, A. Bell, Z.G. Wang, Y. Okada, M. Kawabe, I. Harrison, C.T. Foxon, Competition between band gap and yellow luminescence in undoped GaN grown by MOVPE on sapphire substrate, J. Cryst. Growth 222 (2001) 96–103, https://doi.org/10.1016/S0022-0248(00)00927-1.
[34] P. Jozwik, L. Nowicki, R. Ratajczak, A. Stonert, C. Mieszczynski, A. Turos, K. Morawiec, K. Lorenz, E. Alves, Monte Carlo Simulations of Ion Channeling in Crystals Containing Dislocations and Randomly Displaced Atoms, J. Appl. Phys. 126 (2019) 195107.
[35] A. Caçador, P. Jóźwik, S. Magalhães, J.G. Marques, E. Wendler, K. Lorenz, Extracting defect profiles in ion-implanted GaN from ion channeling, Mater Sci Semicond Process 166 (2023) 107702, https://doi.org/10.1016/j.mssp.2023.107702.
[36] M. Usman, A. Hallén, A. Nazir, Ion implantation induced nitrogen defects in GaN, J. Phys. D: Appl. Phys. 48 (2015) 455107. https://iopscience.iop.org/article/10.1088/0022-3727/48/45/455107.
[37] H.H. Madden, H.P. Hjalmarson, Ion-bombardment-induced changes in the electronic structure of silicon surfaces, J. Vac. Sci. Technol. 20 (1982) 502–505, https://doi.org/10.1116/1.571417.